ORIGINAL PAPERS

Optimizing the shape anisotropy of gold nanoparticles for enhanced light harvesting and photocatalytic applications

Jibin Antony[1] · Sulalit Bandyopadhyay[1] · Jia Yang[1] · Magnus Rønning[1]

Abstract

Hybrid nanoparticles (NP) of bismutite nanodisks (BSC ND) with gold nanoparticles (Au NP) of different aspect ratios (AR), such as spheres, rods and etched rods were synthesized via a facile sonochemical method. To better control the shapes of Au NP deposited on the substrate, these were pre-synthesized prior to the deposition using a modified seed mediated growth method by altering the pH and supersaturation of the growth solution. The shift in the peak position and shape of the localized surface plasmon resonance (LSPR) absorption band associated with fine-tuning of the shape of Au NP, led to enhanced light harvesting capabilities of the hybrid. Introducing shape anisotropy in the NP brought about narrowing of bandgap and lowering of PL intensity in the hybrids, suggesting better electronic contact of the NP with BSC, and effective suppression of recombination effects. Hybrids of BSC with Au nanorods showed 14% improved degradation of methylene blue (MB) dye compared to the hybrids with nanospheres. With this study, we provide a novel promising strategy to maximize the light harvesting capacity of semiconductors by tailoring the AR of Au NP, for improved solar to chemical energy conversion.

Graphical abstract
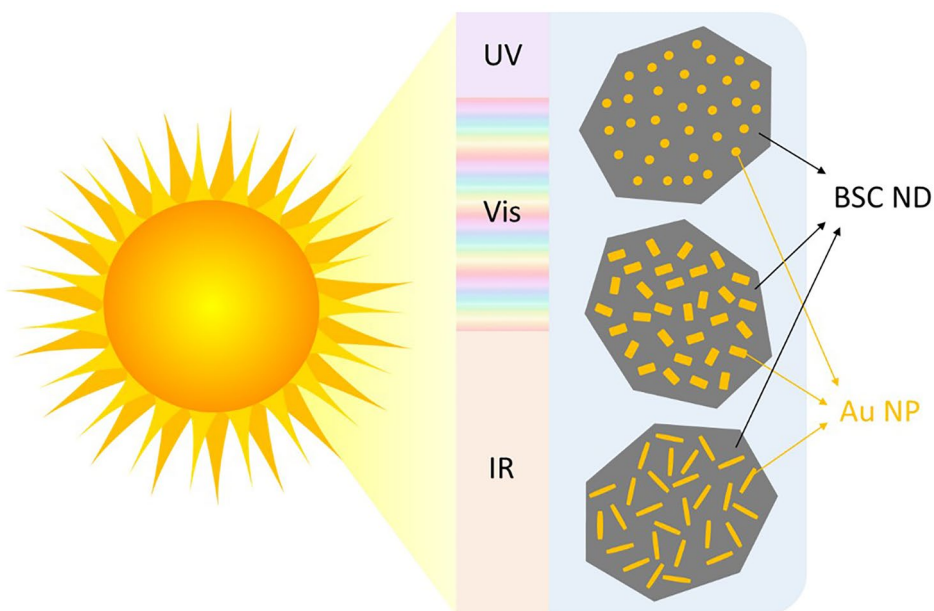
✉ Magnus Rønning
magnus.ronning@ntnu.no

1   Department of Chemical Engineering, Norwegian University
    of Science and Technology, 7491 Trondheim, Norway

🍢 Springer

1 Introduction

Photocatalysis is one of the significant advanced oxidation processes (AOP) used in the mineralization of organic pollutants in the environment. Although a plethora of different photocatalysts have been reported for degrading various organic species, the fact that a majority of these photocatalysts require ultraviolet (UV) light for their excitation, limits their practical use. Bismutite ($Bi_2O_2CO_3$, BSC) nanodisks (ND) consisting of alternating $(Bi_2O_2)^{2+}$ and CO_3^{2-} layered structure is one such catalyst (with a wide bandgap of 3.12 eV) that has recently attracted research attention due to its unique anisotropic crystal structure and internal static electric field, which favors photoinduced charge transfer and separation [1–3]. The quest for photocatalysts being active under sunlight has become significant due to sunlight being a clean and renewable energy source. However, the relatively small fraction of UV light present in solar radiation points toward catalyst engineering strategies aimed at better utilization of the solar spectrum.

Gold nanoparticles (Au NP) have been a topic of intensive investigation owing to their excellent optical properties and localized surface plasmon resonance (LSPR) effect. As a result of LSPR effect, enhanced field strength of the electromagnetic fields near the surface of Au NP can be over 500 times larger than the applied field for structures with sharp edges [4]. Depositing these Au NP on semiconductor substrates has previously been reported to improve the visible light sensitivity and charge separation, thus leading to lower recombination rates and enhanced solar energy collection efficiency [2, 5]. The LSPR properties of Au NP are known to be dependent on the size and shape of the particles among other factors [6]. Several methods have been reported for the deposition of Au NP on the support, such as photodeposition [7], deposition–precipitation [8], incipient wetness impregnation [9], and chemical reduction [10] among others. However, most of these techniques are limited in terms of their ability to control the shape of NP being deposited, thereby restricting the scope of the study to primarily sphere-like particles. Moreover, the NP generated through conventional processes are often polydisperse due to uneven precursor-solution loading caused by gravitational settling and trapping among catalyst particles [11]. This suggests the importance of obtaining hybrids with fine-tuned shapes of NP, to get a clearer understanding of the size-shape effect on the activity. Various strategies have been explored to maximize the light harvesting capacity of these hybrids, such as the formation of plasmonic–semiconductor heterostructures with janus, yolk-shell and dumbbell architectures [12–14]. For instance, a recent study performed by Verbruggen et al. focused on synthesizing a plasmonic 'rainbow' photocatalyst by modifying titania with Au–Ag alloy NP of different compositions, to maximize the spectral response [15]. Although the hybrid catalyst displayed improved utilization of solar spectrum, the modified Turkevich procedure used for the synthesis of the alloy NP limited this study to spherical NP. To achieve improved performance under broadband solar illumination, it is important to synthesize catalysts with simultaneous multiple wavelength plasmonic coupling on semiconductors. The optical properties of NP are known to change dramatically with the incorporation of anisotropy [16]. Thus, optimizing the shape anisotropy of these NP before depositing them on semiconductor substrates is anticipated to improve the light harvesting capacity of the hybrid for photocatalytic applications.

This work aims at synthesizing fine-tuned Au NP of different shapes and obtaining hybrid NP of these with BSC for use in photocatalytic applications. Au NP were synthesized following a seed-mediated growth method previously reported by our group with some modifications [17]. By careful optimization of the synthesis route, by adjusting the pH and supersaturation of the growth solution, shapes with different aspect ratios (AR), such as spheres, rods and etched rods were synthesized. The volume of each particle was kept fairly similar to de-couple the size effect in this study. Nanostructured hybrids of Au NP with BSC were then synthesized using a facile sonochemical approach. The photocatalytic activity of the BSC-Au NP hybrid samples was evaluated in terms of its effectiveness to degrade methylene blue (MB) dye under simulated sunlight at AM 1.5G conditions. The effect of precise tuning of the shape anisotropy of the Au NP on the light harvesting properties of these hybrids is anticipated to pave way for energy efficient solar driven photocatalytic applications.

2 Experimental section

2.1 Synthesis of BSC ND

BSC ND were synthesized following a hydrothermal route as previously reported by Xiao et al. [2]. Briefly, 4.825 g of bismuth (III) nitrate pentahydrate, 2.5 g of urea and 0.387 g of sodium citrate tribasic dihydrate were dispersed in 30 ml of 1 M NaOH by magnetic stirring at 900 rpm for 30 min. This was followed by transferring the suspension into a 100 ml teflon liner of an autoclave. The autoclave was then placed in an oven at 180 ℃ for 6 h, after which it was

brought down naturally to room temperature. The obtained catalyst particles were washed three times each in DI water and ethanol, followed by drying at 80 ℃ for 12 h.

2.2 Synthesis of Au NP

Au NP were synthesized by modifying a seed mediated growth method previously reported by our group [17, 18]. In this method, cetyltrimethyl ammonium bromide (CTAB) coated Au seeds were added to a supersaturated growth solution, which then acted as nucleation sites for the growth to occur.

2.2.1 Synthesis of CTAB coated Au seeds

CTAB coated Au seeds were synthesized by reduction of Au^{3+} ions in solution using $NaBH_4$, a strong reducing agent. In a typical process, 0.2 M CTAB solution was prepared by dissolving 364.5 mg of CTAB in 5 ml DI water at 80 °C and then brought down to 25 °C. 5 ml of 0.5 mM $HAuCl_4 \cdot 3H_2O$ was added to this and kept stirring at 750 rpm for 10 min. This was followed by the addition of 1.6 ml of freshly prepared 3.75 mM $NaBH_4$ under vigorous stirring. The stirring was continued for 2 more minutes after which the seed solution was allowed to age for 30 min.

2.2.2 Growth of CTAB capped Au NP

The growth solution for Au NP was prepared by a sequence of steps as follows. 1.2 g of CTAB (primary surfactant) was initially dissolved in 15 ml DI water at 80 °C to form a transparent solution and then brought down to 35 °C. In case of gold etched nanorods (Au ENR) and gold nanospheres (Au NS), 20 µl of an additional co-surfactant, oleic acid (OA) was also added into the mixture prior to dissolving. To the solution containing surfactant(s), 750 µl of freshly prepared 4 mM $AgNO_3$ solution was added, followed by 15 min of stirring. Thereafter, 15 ml of 1 mM $HAuCl_4 \cdot 3H_2O$ was added to the mixture and kept stirring for another 15 min. In case of Au ENR and Au NS, the pH of the growth solution was modified at this point using different concentrations of NaOH. Gold nanorods (Au NR) were synthesized at natural pH conditions [pH = 3.6 before addition of ascorbic acid (AsA)]. It is to be noted that the concentration of the NaOH used in adjusting the pH plays a significant role in the shape selectivity as it affects the supersaturation of the growth solution. For Au ENR synthesis, pH of the growth solution was adjusted to 9.8 using 0.1 M NaOH and in case of Au NS, 1 M NaOH was used to adjust the pH to 10.7. Subsequently, 135 µl of 130 mM AsA was added under vigorous stirring (1100 rpm). This was followed by the addition of 96 µl of 30-min aged CTAB coated Au seeds in case of Au NR and Au ENR after which the stirring was stopped. However, Au

seeds were not used in Au NS synthesis as these showed spontaneous growth right after adding AsA, thus denoting primary nucleation. The Au NP solutions were allowed to stay overnight at 35 °C and later collected by centrifuging twice at 11,000 rpm for 20 min to remove the excess surfactant. The bottom product was then re-dispersed in 10 ml DI water for each type of NP.

2.3 Normalizing the concentration of Au NP

As reported in our previous work [17], altering the pH of the growth solution affects the growth kinetics and as a result would lead to different concentrations of Au NP in the final suspension. For estimating the concentration of the different batches, a small fraction from the 10 ml Au NP dispersion was digested in aqua regia followed by dilution. This was then analyzed in a Microwave Plasma Atomic Emission Spectrometer (MP-AES 4210, Agilent) to obtain the concentration. To normalize the weight fraction of different shapes of Au NP being deposited on BSC, 2 batches of Au NR (10 ml each) were combined to make a 20 ml colloidal suspension (this was done to account for the low weight fraction of gold obtained for Au NR). However, due to improved weight fractions of gold obtained in case of Au NS and Au ENR, each of these suspensions were diluted to 20 ml by adding 10 ml of DI water.

2.4 Synthesis of BSC/Au hybrid NP

BSC/Au hybrid NP were synthesized by a facile sonochemical method in presence of methanol (MeOH). In a typical synthesis process for depositing 1 wt% Au, different weights of BSC ND (depending on the shapes of Au NP being deposited; Au NS-248 mg, Au ENR-215 mg, Au NR-210 mg) was dispersed in 25 ml MeOH under ultrasonication (Elmasonic S30H, 37 kHz, 280 W) for 5 min. The Au NP batches (20 ml) were also ultrasonicated (37 kHz, 280 W) for 5 min to ensure good dispersion of the NP in solution. The Au NP batches were then added dropwise to the BSC dispersion under magnetic stirring at 1000 rpm. This was followed by ultrasonication of the mixture for 15 min to obtain the hybrid NP. These were separated from solution via centrifuging at 11,000 rpm for 10 min and later cleaned one more time with ethanol before drying these particles overnight at 70 °C.

3 Results and discussion

3.1 Morphology characterization

The morphology of BSC ND was analyzed using S(T)EM and is shown in Fig. S1. The ND had an average size of 330 ± 130 nm (represented as average $\pm$ standard deviation)
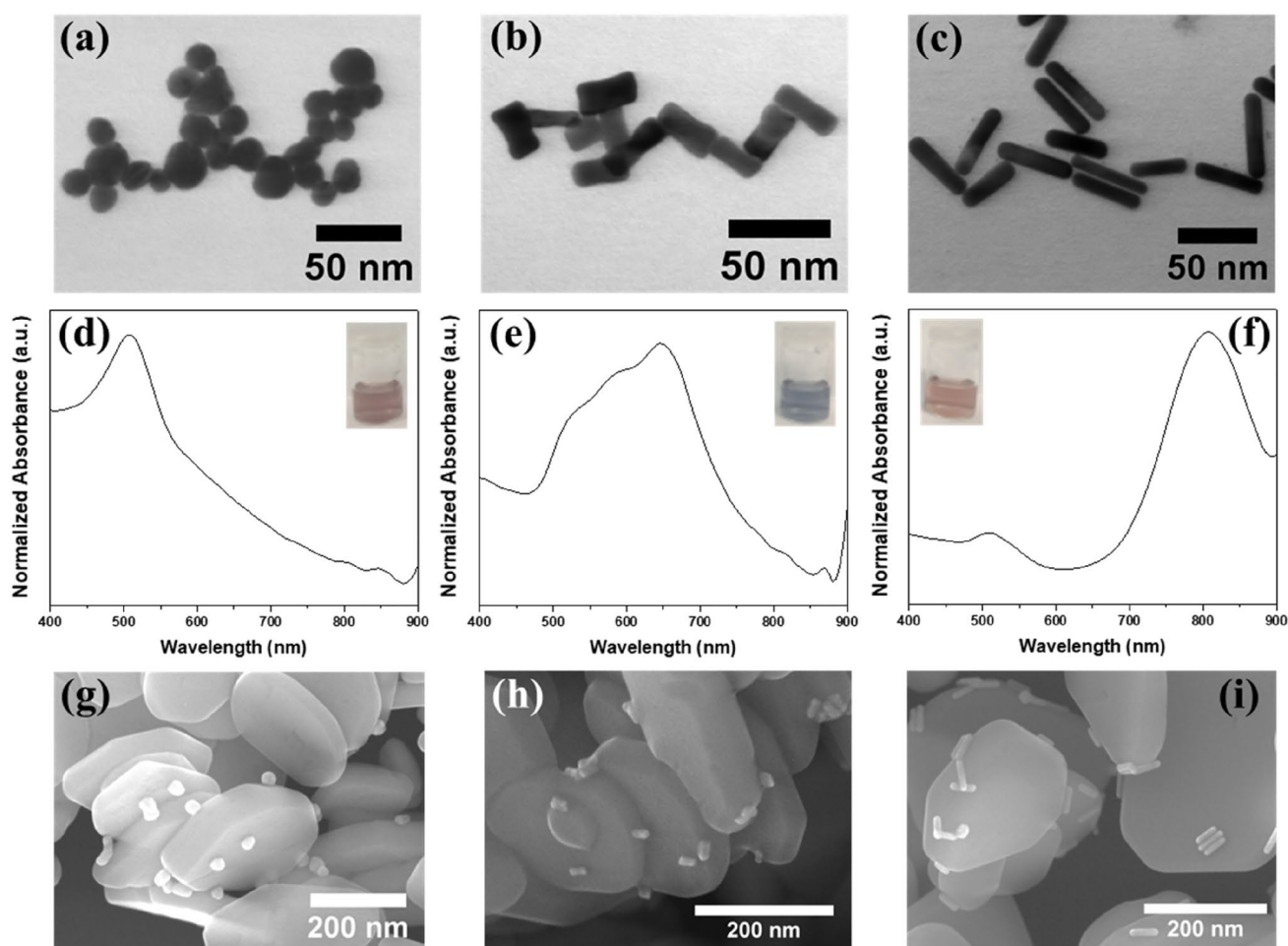
Fig. 1 Different shapes of Au NP synthesized using a modified seed-mediated growth approach, **a** NS, **b** ENR, **c** NR; the absorbance spectra of these different shapes are shown in (**d**), (**e**) and (**f**), respectively, the inset shows the color of an aqueous colloidal dispersion of the NP; hybrid NP obtained by sonochemical deposition of the Au NP on BSC ND are shown in (**g**), (**h**) and (**i**), respectively

and thickness of 50 ± 8 nm, and the shapes were in agreement with the structures previously reported by Xiao et al. [2]. Figure 1a–c shows the different shapes of Au NP obtained from the modified seed-mediated growth. The spherical nanoparticles (Au NS) in Fig. 1a had dimensions of 18 ± 5 nm; the etched nanorods (Au ENR) in Fig. 1b had long axes dimension of 26 ± 4 nm and a short axes dimension of 13 ± 3 nm; the nanorods in Fig. 1c had long axes dimension of 42 ± 6 nm and a short axes dimension of 10 ± 1 nm, respectively. AR being a parameter which better describes the anisotropy in terms of ratio of long axes to short axes of the NP is shown in Fig. S2. Au NS showed an AR of 1 ± 0.1, thus denoting almost no anisotropy in the spherical NP. Au ENR and Au NR had AR of 2.2 ± 0.4 and 4.1 ± 0.5, respectively. Precise tuning of the seed-mediated growth route was achieved by altering the pH and supersaturation of the growth solution to achieve different shapes, but with similar particle volumes. This was done to de-couple the size effect in this study. The approximate volume of the

different shapes of Au NP was calculated and is shown in Fig. S3.

Figure 1d–f shows the absorbance spectra for an aqueous dispersion of the different shaped Au NP and their corresponding color in the inset figures. It can be noted that Au NS showed a single LSPR absorbance peak at a wavelength of 508 nm. This was in congruence with previous works on Au NS, where the peak position and broadening have been reported to be functions of particle size and polydispersity among other factors [19]. ENR showed a shift in the LSPR absorbance compared to NS, with the main peak at 646 nm and two shoulders at 525 nm and 585 nm, respectively; NR showed two distinct absorbance peaks at 508 nm and 807 nm corresponding to the transverse and longitudinal axes, respectively. The longitudinal peak position of Au NR is known to shift with change in AR, higher AR leading to longitudinal peaks at longer wavelengths [20]. The spectral irradiance of the solar simulator (as provided by the manufacturer ScienceTech) is shown in Fig. S4 to depict the

overlap of Au NP absorbance spectra with the intensity of irradiated light. The light intensity of the solar simulator was observed to be quite broad in the visible and near-infrared regions as seen from the percentage of intensities at specific wavelengths. A good overlap of the spectral range of incident photon with the LSPR absorbance of the plasmonic metal provides a useful tool to predict the enhanced properties of the hybrid NP [21].

The concentration of different Au batches was estimated using MP-AES, and the yields (denoting weight fraction of Au obtained as NP from the initial Au precursor concentration) obtained for NS, ENR and NR were $85 \pm 4\%$, $74 \pm 3\%$ and $36 \pm 2\%$. A higher supersaturation of growth solutions for NS and ENR leads to faster reduction of Au^{1+} (obtained via reduction of Au^{3+} in the presence of reducing agent AsA) ions to Au^0, hence giving better yields[17]. Figure 1g–i shows SEM images of hybrid NP obtained by sonochemical deposition of different shapes of Au NP on BSC ND.

The Au NP were observed to be tightly bound to the BSC ND indicating strong metal support interaction, and retained its shape even after deposition. Figure S5 shows images of powder samples of the hybrid particles.

The elemental composition of the hybrid samples was analyzed in an EDX spectrometer, and the results are tabulated in Table S1. A representative EDX elemental map of BSC-AuNR is shown in Fig. S6. Since there were few areas of the substrate with non-uniform gold deposition, MP-AES was used in conjunction with EDX to get a better estimate of the gold loading in the hybrid. A similar weight fraction of deposited gold obtained from MP-AES for the different hybrid samples (as shown in Fig. S7) ensured complete deposition of the pre-synthesized gold on BSC ND.

The powder XRD patterns of BSC and the hybrid samples are shown in Fig. 2a. The diffraction peaks of the hybrids were in alignment with BSC and were indexed to tetragonal bismutite ($Bi_2O_2CO_3$) with $a = b = 3.867$ Å; $c = 13.686$ Å;
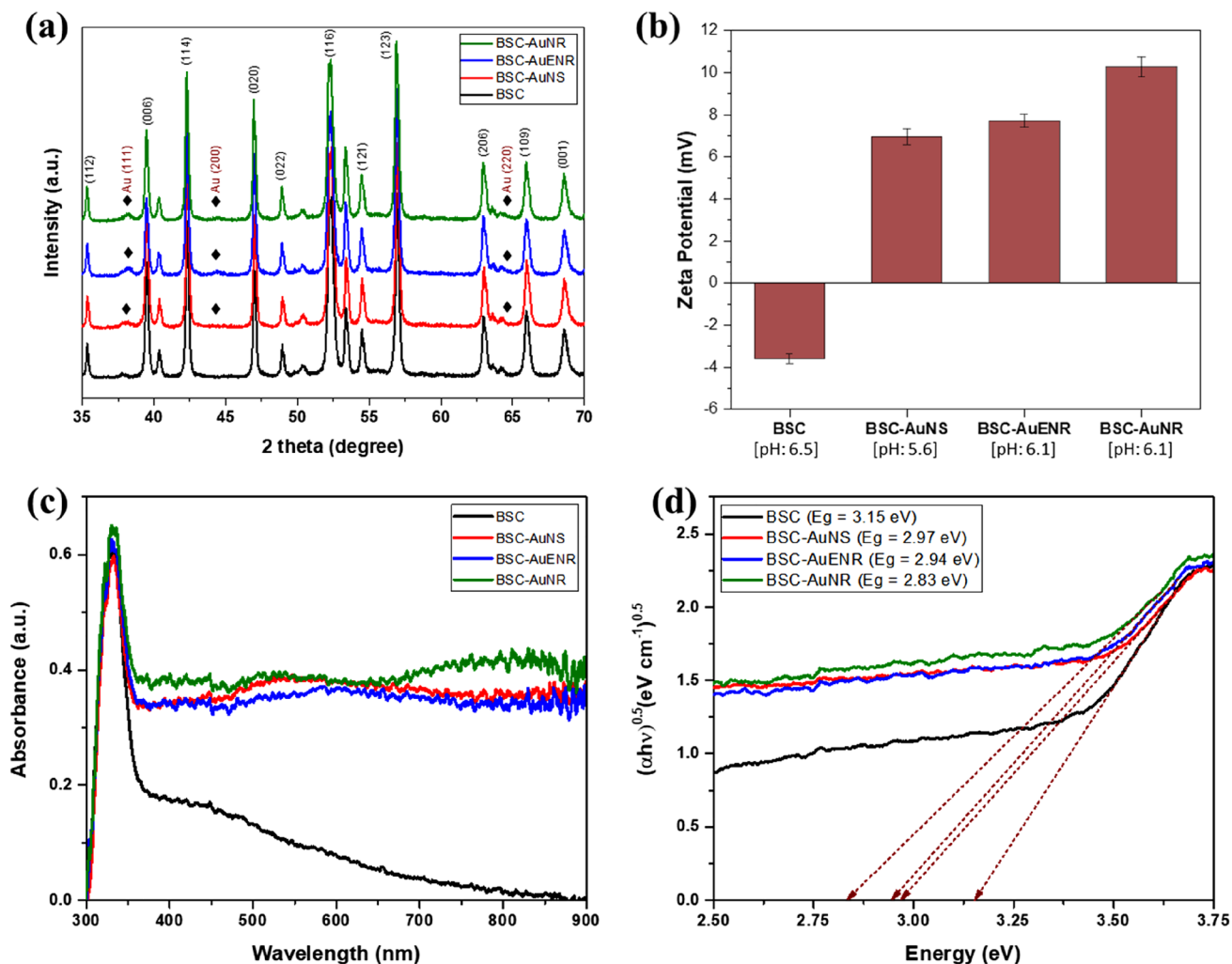

Fig. 2 a XRD patterns-diamond markers represent diffraction from crystal planes of metallic Au, **b** zeta potential at natural pH, **c** UV–Vis absorption spectra, and **d** Tauc plot showing the optical bandgap of the hybrid samples

and space group I4/mm; JCPDS Card No. 41-1488. The peaks from BSC were observed to be sharp indicating high crystallinity of the sample. In addition to the peaks from BSC, some broad peaks (indicated by diamond markers in Fig. 2a) could be detected for the hybrids at 38.2°, 44.4° and 64.6°, which could be assigned to (111), (200) and (220) crystal planes of metallic Au with cubic structure (JCPDS Card No. 04-0784). The zeta potential representing surface charge of the particles was performed at natural pH in a catalyst suspension of 200 mg/L and is shown in Fig. 2b. BSC ND which has an isoelectric point below 3, was observed to have negative zeta potential at its natural pH of 6.5, due to deprotonation of adsorbed hydroxyl groups present on the surface [1]. In contrast, the hybrid particles showed positive values of zeta potential due to the presence of CTAB stabilizing the Au NP. An increase in the absolute value of zeta potential could also be observed for the hybrids containing Au ENR and Au NR. This could be due to higher fraction of surface Au atoms present in these structures (since the particle volumes of different shapes were kept nearly similar).

The light harnessing capacity of the hybrid samples was compared by obtaining the UV–Vis diffuse reflectance spectra (DRS), as shown in Fig. 2c. As can be observed, pristine BSC displayed an absorption edge at approximately 370 nm and exhibited very low absorbance intensity at wavelengths above 370 nm, indicating their visible light inertness. The hybrid samples were observed to show additional absorbance peaks corresponding to the surface plasmon band of the particles being deposited, thereby leading to improved light absorption in the visible spectrum. In case of BSC-AuNR hybrid, the absorbance was seen to extend to the near infrared region as a result of the longitudinal peak of Au NR. However, BSC-AuENR was observed to show the least absorbance, which could be due to the slightly lower weight fraction of deposited Au on these hybrids as obtained from MP-AES (Fig. S7). The optical bandgap of the hybrids was obtained using Tauc plots, as shown in Fig. 2d. BSC ND displayed a bandgap of 3.15 eV which was consistent with literature [2]. Narrowing of the bandgap could be observed for the BSC-Au hybrids with BSC-AuNR displaying the most narrow bandgap of 2.83 eV. This could be due to a systematic red shift of the absorption edge observed for the hybrids with increasing anisotropy of the particles being deposited [22].

PL spectra of the hybrid samples were obtained to get a better understanding of the transfer, separation and recombination processes of the photogenerated electron–hole pairs. Figure S8 shows the PL intensity comparison performed at an excitation wavelength of 350 nm and emission scans between 365 and 700 nm. A significant quenching in PL intensity could be observed in the hybrids with incorporation of Au NP, with the intensities decreasing in the order BSC > BSC-AuNS > BSC-AuENR > BSC-AuNR, thus indicating least charge carrier recombination effects in BSC-AuNR [23]. This could indicate the migration of excited electrons in the conduction band of BSC to the new Fermi energy level of the hybrid, which would act as trapping sites for the electrons (electron sinks), thereby improving charge separation [24, 25]. The least PL intensity observed for BSC-AuNR hybrid could be a result of stronger electronic contact of Au NR on the BSC surface, due to higher surface fraction of gold with increasing AR.
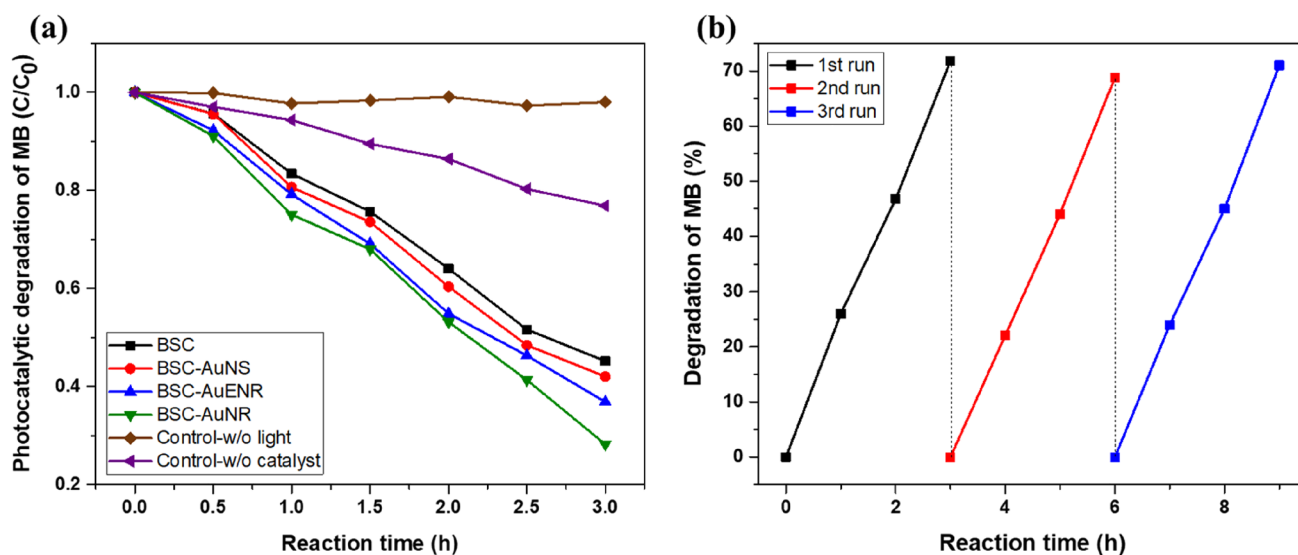

Fig. 3 a Comparison of photocatalytic MB degradation between different hybrid samples along with control experiments, **b** catalyst stability analysis showing three consecutive runs with BSC-AuNR hybrid; the stability runs were performed in borosilicate glass reactors by reducing the reaction volume in subsequent runs, but fixing the catalyst concentration; aliquots were withdrawn every hour

Photocatalytic comparison studies were performed using the hybrid catalysts for MB degradation, as shown in Fig. 3a. The concentration of residual dye in the aliquots were calculated using the calibration curve for MB, as shown in Fig. S9. Enhanced light harvesting capacity of the hybrids with Au NR at longer wavelengths of the solar spectrum could be observed in terms of improved activity for MB degradation. The degradation percentage of MB after 3 h of reaction was found to be 54.8%, 57.9%, 63.1% and 71.8% for BSC, BSC-AuNS, BSC-AuENR and BSC-AuNR, respectively. A 14% improvement in degradation observed in hybrid structures with Au NR compared to Au NS could be due to the synergetic effects of superior visible light absorption, improved charge–carrier separation, and stronger near-field enhancements. Obtaining anisotropic particles with higher AR, yet smaller in size could lead to an increase in the surface fraction of gold, which is expected to further improve the performance of the hybrid. Control experiments were performed both in the absence of catalyst (with light irradiation) and absence of light (with photocatalyst), as shown in Fig. 3a. Insignificant MB degradation observed in these reactions verified the effectiveness of the hybrid catalyst. The degradation performance could be described by the pseudo-first-order kinetic model:

$$-\ln(C/C_0) = k_{\text{app}}t \qquad (1)$$

where C and C_0 denote the concentration of MB dye at time 't' and after attaining adsorption–desorption equilibrium, respectively, and k_{app} refers to the apparent pseudo-first-order kinetic constant (h^{-1}). The plot of $\ln(C_0/C)$ versus time shown in Fig. S10 exhibited a good linear fit with the R^2 values and k_{app} listed in Table S2. BSC-AuNR samples showed the highest k_{app} value, further verifying the above inference. The photocatalytic performance of the hybrid samples was also tested in the visible light spectrum using a UV light cutoff filter (cuts off wavelength < 400 nm) and is shown in Fig. S11. Although some degradation could be observed in all the samples, it was difficult to observe any particular trend or improvements between the samples in the visible light emission window. This might indicate that a plasmonic excitation brought about by absorption of visible light alone was not sufficient to activate the BSC particles in our study.

The photocatalytic stability of the BSC-AuNR hybrid was tested to determine its reusability, by performing three consecutive MB degradation experiments with the spent catalyst obtained after each run. The spent catalyst was centrifuged and cleaned once in ethanol, and later dried at 70 °C overnight. Good consistency in the performance runs with a final degradation of $70.5 \pm 1.3\%$ as observed from Fig. 3b proved good stability of the hybrid.

A plausible mechanism for the plasmonic enhancement observed in this study could be assigned to a synergistic effect of improved charge–carrier separation and stronger near-field enhancements with the incorporation of anisotropic Au NP. Sonochemical deposition of plasmonic NP have been reported in literature to obtain strong contact with the semiconductor particles with a Schottky junction [26, 27]. When solar light is irradiated on the hybrid NP, the electrons in the valence band of BSC gets excited to the conduction band. The recombination of these electrons with the holes in the valence band could be delayed by their migration to the newly formed Fermi energy level of the hybrid NP, where they reduce the dissolved oxygen to form superoxide anion radical ($\cdot O_2^-$) [27]. At the same time, holes in the valence band of BSC are captured by surface OH^- groups or adsorbed H_2O to produce hydroxyl radical ($\cdot OH^-$). These radicals would oxidize MB due to their high redox potentials. The Schottky barrier at the equilibrated interface of the hybrid would limit the reverse metal to semiconductor transfer of electrons, thereby improving the separation efficiency of photo-excited charge carriers. Near-field enhancements due to strong plasmon-induced electric field near the metal surface is known to significantly enhance the rate of photoexcitation in the semiconductor [28]. The presence of anisotropy leads to stronger near-field enhancement effects, and this could support the improved performance of BSC-AuNR [29]. Hot electron injection from Au NP to the conduction band of BSC did not seem to have a prominent effect in this study. This could be verified in terms of insignificant activity improvements observed for the hybrids in the visible light spectrum. A restricted interface area between the Au NP and BSC due to surface deposition might lead to poor transport of hot electrons compared to when the NP is partially embedded into the semiconductor [30]. The small size of Au NP used in this study could also suggest that the improvements caused through resonant scattering was not relevant here [28, 31].

It should be noted that even though MB is widely used as a target contaminant for photocatalytic studies, its use has been debated as it could also induce a photosensitization mechanism along with photocatalysis. However, the control experiments performed under identical conditions along with insignificant improvements observed for the hybrids in presence of visible light exclude the presence of a dye-sensitization mechanism in this study [32, 33].

4 Conclusions

This work reports a novel approach for enhanced light harvesting for photocatalytic applications by post deposition of anisotropic Au NP on BSC ND. Fine tuning the shape of Au NP was achieved by a modified seed-mediated growth method by adjusting the pH and supersaturation of the growth solution. In comparison with spherical Au NP that has been widely studied in literature, the symmetry breaking of these NP leading to anisotropic morphologies was observed to enhance the

light harvesting properties and photoredox efficiencies of the hybrid. Bandgap narrowing and lowering of PL intensity could be observed with increasing anisotropy of the deposited NP, which indicates a lowering of the Fermi energy level of the hybrid along with superior charge–carrier separation efficiencies. Further optimizing the shape of the deposited Au NP on BSC ND or depositing a mixture of different shapes of Au NP is anticipated to provide viable solutions for more efficient utilization of the solar spectrum.

Data availability The datasets generated during and/or analysed during the current study are available from the corresponding author on justified request.

Declarations

Conflict of interest The authors have no competing interests to declare that are relevant to the content of this article.

References

1. Selvamani, T., Raj, B. G. S., Anandan, S., Wu, J. J., & Ashokkumar, M. (2016). Synthesis of morphology-controlled bismutite for selective applications. *Physical Chemistry Chemical Physics, 18*, 7768–7779.

2. Xiao, C., Hu, H., Zhang, X., & MacFarlane, D. R. (2017). Nanostructured gold/bismutite hybrid heterocatalysts for plasmon-enhanced photosynthesis of ammonia. *ACS sustainable chemistry & engineering, 5*, 10858–10863.

3. Xu, R., Su, M., Liu, Y., Chen, Z., Ji, C., Yang, M., Chang, X., & Chen, D. (2020). Comparative study on the removal of different-type organic pollutants on hierarchical tetragonal bismutite microspheres: adsorption, degradation and mechanism. *Journal of Cleaner Production, 242*, 118366.

4. Chen, X., Zhu, H. Y., Zhao, J. C., Zheng, Z. F., & Gao, X. P. (2008). Visible-light-driven oxidation of organic contaminants in air with gold nanoparticle catalysts on oxide supports. *Angewandte Chemie, 120*, 5433–5436.

5. Li, Q., Hao, X., Guo, X., Dong, F., & Zhang, Y. (2015). Controlled deposition of Au on (BiO) 2 CO 3 microspheres: the size and content of Au nanoparticles matter. *Dalton Transactions, 44*, 8805–8811.

6. Takahiro, K., Naya, S.-I., & Tada, H. (2014). Highly active supported plasmonic photocatalyst consisting of gold nanoparticle-loaded mesoporous titanium (IV) oxide overlayer and conducting substrate. *The Journal of Physical Chemistry C, 118*, 26887–26893.

7. Li, D., McCann, J. T., Gratt, M., & Xia, Y. (2004). Photocatalytic deposition of gold nanoparticles on electrospun nanofibers of titania. *Chemical Physics Letters, 394*, 387–391.

8. Hammer, N., Kvande, I., Xu, X., Gunnarsson, V., Tøtdal, B., Chen, D., & Rønning, M. (2007). Gunnarsson, B. Tøtdal, D. Chen, M. Rønning, Au–TiO2 catalysts on carbon nanofibres prepared by deposition-precipitation and from colloid solutions. *Catalysis today, 123*, 245–256.

9. Delannoy, L., El Hassan, N., Musi, A., Le To, N. N., Krafft, J.-M., & Louis, C. (2006). Preparation of supported gold nanoparticles by a modified incipient wetness impregnation method. *The Journal of Physical Chemistry B, 110*, 22471–22478.

10. Bu, T.-A., Hao, Y.-C., Gao, W.-Y., Su, X., Chen, L.-W., Zhang, N., & Yin, A.-X. (2019). Promoting photocatalytic nitrogen fixation with alkali metal cations and plasmonic nanocrystals. *Nanoscale, 11*, 10072–10079.

11. Li, J., & Zeng, H. C. (2006). Preparation of monodisperse Au/TiO2 nanocatalysts via self-assembly. *Chemistry of Materials, 18*, 4270–4277.

12. Jia, H., Du, A., Zhang, H., Yang, J., Jiang, R., Wang, J., & Zhang, C.-Y. (2019). Site-selective growth of crystalline ceria with oxygen vacancies on gold nanocrystals for near-infrared nitrogen photofixation. *Journal of the American Chemical Society, 141*, 5083–5086.

13. Seh, Z. W., Liu, S., Low, M., Zhang, S. Y., Liu, Z., Mlayah, A., & Han, M. Y. (2012). Janus Au-TiO2 photocatalysts with strong localization of plasmonic near-fields for efficient visible-light hydrogen generation. *Advanced Materials, 24*, 2310–2314.

14. Sun, H., He, Q., Zeng, S., She, P., Zhang, X., Li, J., & Liu, Z. (2017). Controllable growth of Au@ TiO 2 yolk–shell nanoparticles and their geometry parameter effects on photocatalytic activity. *New Journal of Chemistry, 41*, 7244–7252.

15. Verbruggen, S. W., Keulemans, M., Goris, B., Blommaerts, N., Bals, S., Martens, J. A., & Lenaerts, S. (2016). Plasmonic 'rainbow' photocatalyst with broadband solar light response for environmental applications. *Applied Catalysis B: Environmental, 188*, 147–153.

16. Eustis, S., & El-Sayed, M. A. (2006). Why gold nanoparticles are more precious than pretty gold: noble metal surface plasmon resonance and its enhancement of the radiative and nonradiative properties of nanocrystals of different shapes. *Chemical society reviews, 35*, 209–217.

17. Raghunathan, K., Antony, J., Munir, S., Andreassen, J.-P., & Bandyopadhyay, S. (2020). Tuning and tracking the growth of gold nanoparticles synthesized using binary surfactant mixtures. *Nanoscale Advances, 2*, 1980–1992.

18. Bandyopadhyay, S., McDonagh, B. H., Singh, G., Raghunathan, K., Sandvig, A., Sandvig, I., Andreassen, J.-P., & Glomm, W. R. (2018). Growing gold nanostructures for shape-selective cellular uptake. *Nanoscale Research Letters, 13*, 254.

19. Link, S., & El-Sayed, M. A. (1999). Size and temperature dependence of the plasmon absorption of colloidal gold nanoparticles. *The Journal of Physical Chemistry B, 103*, 4212–4217.

20. Han, C., Qi, M.-Y., Tang, Z.-R., Gong, J., & Xu, Y.-J. (2019). Gold nanorods-based hybrids with tailored structures for photoredox catalysis: fundamental science, materials design and applications. *Nano Today, 27*, 48–72.

21. Kochuveedu, S. T., Jang, Y. H., & Kim, D. H. (2013). A study on the mechanism for the interaction of light with noble metal-metal oxide semiconductor nanostructures for various photophysical applications. *Chemical Society Reviews, 42*, 8467–8493.

22. Ahmad, M., Rehman, W., Khan, M. M., Qureshi, M. T., Gul, A., Haq, S., Ullah, R., Rab, A., & Menaa, F. (2021). Phytogenic fabrication of ZnO and gold decorated ZnO nanoparticles for photocatalytic degradation of Rhodamine B. *Journal of Environmental Chemical Engineering, 9*, 104725.

23. Patnaik, S., Martha, S., Madras, G., & Parida, K. (2016). The effect of sulfate pre-treatment to improve the deposition of Au-nanoparticles in a gold-modified sulfated gC 3 N 4 plasmonic photocatalyst towards visible light induced water reduction reaction. *Physical Chemistry Chemical Physics, 18*, 28502–28514.

24. Gupta, B., Melvin, A. A., Matthews, T., Dash, S., & Tyagi, A. (2016). TiO2 modification by gold (Au) for photocatalytic hydrogen (H2) production. *Renewable and Sustainable Energy Reviews, 58*, 1366–1375.

25. Zhu, H., Yuan, X., Yao, Q., & Xie, J. (2021). Shining photocatalysis by gold-based nanomaterials. *Nano Energy, 88*, 106306.

26. Buapoon, S., Phuruangrat, A., Dumrongrojthanath, P., Thongtem, T., & Thongtem, S. (2021). Sonochemical synthesis and characterization of Ag/ZnO heterostructure nanocomposites and their photocatalytic efficiencies. *Journal of Electronic Materials, 50*, 4524–4532.

27. Jung, W.-S., Park, S.-H., Kadam, A. N., Kim, H., & Lee, S.-W. (2020). Direct hydrothermal synthesis of amine-functionalized cubic hematite (C-Fe 2 O 3) and sonochemical deposition of nano-sized Au for its application as a visible-light photocatalyst. *Dalton Transactions, 49*, 2924–2932.

28. Ninakanti, R., Dingenen, F., Borah, R., Peeters, H., & Verbruggen, S. W. (2022). Plasmonic Hybrid Nanostructures in Photocatalysis: Structures, Mechanisms, and Applications. *Topics in Current Chemistry, 380*, 1–62.

29. Borah, R., & Verbruggen, S. W. (2020). Silver–gold bimetallic alloy versus core–shell nanoparticles: Implications for plasmonic enhancement and photothermal applications. *The Journal of Physical Chemistry C, 124*, 12081–12094.

30. Ma, X. C., Dai, Y., Yu, L., & Huang, B. B. (2016). Energy transfer in plasmonic photocatalytic composites. *Light: Science & Applications, 5*, e16017.

31. Verbruggen, S. W. (2015). TiO2 photocatalysis for the degradation of pollutants in gas phase: From morphological design to plasmonic enhancement. *Journal of Photochemistry and Photobiology C: Photochemistry Reviews, 24*, 64–82.

32. Ohtani, B. (2008). Preparing articles on photocatalysis—Beyond the illusions, misconceptions, and speculation. *Chemistry Letters, 37*, 216–229.

33. Wang, D., Pillai, S. C., Ho, S.-H., Zeng, J., Li, Y., & Dionysiou, D. D. (2018). Plasmonic-based nanomaterials for environmental remediation. *Applied Catalysis B: Environmental, 237*, 721–741.